

What lies beyond the horizon of a holographic p-wave superconductor

Lewis Sword and David Vegh

*Centre for Theoretical Physics, Department of Physics and Astronomy
Queen Mary University of London, 327 Mile End Road, London E1 4NS, UK*

Email: l.sword@qmul.ac.uk, d.vegh@qmul.ac.uk

October 12, 2022

Abstract

We study the planar anti-de Sitter black hole in the p-wave holographic superconductor model. We identify a critical coupling value which determines the type of phase transition. Beyond the horizon, at specific temperatures flat spacetime emerges. Numerical analysis close to these temperatures demonstrates the appearance of a large number of alternating Kasner epochs.

Contents

1	Introduction	2
2	Holographic p-wave superconductor	3
2.1	Action and equations of motion	3
2.2	Boundary conditions	4
3	Thermodynamics	6
3.1	Phase transitions	6
3.2	Grand potential and entropy analysis	8
4	Black hole interior	14
4.1	Josephson oscillations	14
4.2	Kasner regime	15
4.3	Near-oscillatory Kasner epoch	18
5	Conclusion	22

1 Introduction

The AdS/CFT correspondence [1, 2, 3], otherwise known as gauge-gravity duality, introduced a method to inspect strongly coupled theories. From it emerged a dictionary relating fields in bulk spacetime to operators on its boundary. Using this correspondence, the gravitational dual of a superconductor, known as a holographic superconductor, was discovered [4, 5, 6]. By spontaneously breaking an abelian gauge symmetry of a charged scalar field in Schwarzschild-AdS spacetime, one produces a non-trivial expectation value for the scalar field, which corresponds to a non-zero condensate developing on the boundary¹. These original models used a simple $U(1)$ charged scalar boson to introduce a condensate (scalar “hair”), however other bosonic condensate models are possible such as p-wave superconductors where a charged vector field is employed utilising $SU(2)$ gauge theory². This takes a $U(1)$ subgroup as electromagnetism and allows the gauge bosons that are charged under the $U(1)$ to condense. The original p-wave model was presented in [8] followed by a top-down, string theory approach in [9, 10, 11] and backreaction on the metric was accounted for in [12, 13].

In both vector and scalar condensate cases, the identification of the gravitational counterparts of superconductors is attributed to a condensing field and a black hole spacetime with a given Hawking temperature in the bulk. This topic has garnered great interest since its inception. The exploration of the black hole interior began with [14, 15] and was extended to the full scalar field holographic superconductor model in [16]. Numerous interesting phenomena were observed in the interior including Kasner geometries³, collapse of the Einstein-Rosen (ER) bridge and Josephson oscillations. The interior has subsequently been subjected to further study. This includes the introduction of additional field content and variation of coupling parameters [19, 20, 21, 22, 23], use of alternative black hole solutions [24, 25, 26], analysis of RG flows [27, 28], as well as the construction of “no inner-horizon” theorems [29]. Investigation of the interior solutions for the p-wave model are now also being explored, with the analogous changes in geometry and matter fields being observed [30].

This paper aims to show the interesting changes in interior geometry by exploring the parameter space of the p-wave superconductor. The key result is that for a special selection of parameters, the numerical solutions appear to imply that the interior geometry becomes flat. Not only that, but either side of this parameter selection, the geometry becomes almost oscillatory in Kasner universes.

The outline of the paper is as follows. Section 2 introduces the holographic p-wave superconductor model. Here the equations of motion are established, followed by details of the numerical procedure to solve them. We also state the equations’ scaling symmetries, as well as the horizon and UV series expansions as governed by the necessary boundary conditions. Section 3 puts the numerical solutions to use, by exploring the exterior of the black hole. We first analyse the field content in the exterior confirming that the solutions satisfy the correct boundary conditions. Under vanishing condensate, we enter normal phase as verified by the metric returning to that of a Reissner-Nordström spacetime. Following this, upon various choices of the model parameters, the phase diagrams for the holographic superconductor are produced. The phase curves imply that a critical g_{YM} coupling exists, which differentiates between first and second order transitions. This is confirmed by analysis of the grand potential derived from the Euclidean action as well as the entropy. Section 4 explores the interior

¹On the boundary the $U(1)$ symmetry that is spontaneously broken in the superconducting phase is a global symmetry, hence is more accurately described as a superfluid.

²In addition to the scalar and vector condensates, d-wave superconductors based on spin-2 condensates have also been the subject of similar holographic analysis [7].

³In the context of cosmology, Kasner regimes have also been investigated in [17, 18].

and presents our main findings. We begin by studying the interior field content close to the horizon, which demonstrates typical behaviour previously seen such as the Josephson oscillations and ER bridge collapse. The focus then turns to specific points in the parameter space. Here the key finding is that at certain values the interior geometry appears to become flat while slight deviations away from this point lead to a highly oscillatory geometry comprised of individual Kasner universes for a given bulk radius. Section 5 presents a summary of our findings and discusses possible future endeavours.

At the time of review, it has come to our attention that [31] discusses infinite oscillations in a scalar field model and [32] presents results for transitions between different Kasner epochs using a top-down, scalar holographic superconductor model.

2 Holographic p-wave superconductor

2.1 Action and equations of motion

The model used is a $(3 + 1)$ -dimensional, $SU(2)$ Yang-Mills theory with Einstein-Hilbert and cosmological constant terms allowing us to obtain asymptotically anti-de Sitter (AdS) geometry. The action is

$$I = \frac{1}{\kappa_{(4)}^2} \int d^{3+1}x \sqrt{-g} \left[R - 2\Lambda - \frac{1}{4} \text{Tr} [F_{\mu\nu} F^{\mu\nu}] \right] = \int d^{3+1}x \sqrt{-g} \mathcal{L}, \quad (1)$$

with Lagrangian \mathcal{L} and field strength

$$F_{\mu\nu}^a = \nabla_\mu A_\nu^a - \nabla_\nu A_\mu^a + g_{\text{YM}} \epsilon^{abc} A_\mu^b A_\nu^c. \quad (2)$$

Here, R is the Ricci scalar, $\Lambda = -3/L^2$ is the cosmological constant with L the radius of curvature of AdS, g is the determinant of the metric, $\kappa_{(4)}$ is the four-dimensional gravitational constant, $g_{\text{YM}} = \hat{g}_{\text{YM}}/\kappa_{(4)}$ where \hat{g}_{YM} is the standard Yang-Mills coupling and ϵ^{abc} is the Levi-Civita symbol. A_μ^a represent the Lie-algebra valued gauge fields, defined in form notation as $A = A_\mu^a \tau^a dx^\mu$ where τ^a are the generators of the $SU(2)$ algebra defined by the Pauli matrices, σ^a , as $\tau^a = \sigma^a/2i$. In the above, ‘‘Tr’’ refers to the trace over Lie indices and in the convention used, $\text{Tr}[\tau^a \tau^b] = \frac{1}{2} \delta^{ab}$. For example $\frac{1}{4} \text{Tr} [F_{\mu\nu} F^{\mu\nu}] = \frac{1}{8} \sum_a F_{\mu\nu}^a F^{a\mu\nu}$, where for $SU(2)$, the three generators are denoted by $a = 1, 2, 3$ and satisfy Lie bracket $[\tau^a, \tau^b] = \epsilon^{abc} \tau^c$. Under the identification of $\hat{A}_\mu = A_\mu/g_{\text{YM}}$ we may think of g_{YM} as a measure of the backreaction: for large g_{YM} we enter the probe limit. This limit essentially scales away the effect of the gauge field such that it has negligible contributions to the gravitational equations of motion.

Varying the action of (1) with respect to the metric, $g_{\mu\nu}$, and the Yang-Mills gauge field, A_μ , the resulting equations of motion are

$$R_{\mu\nu} - \frac{1}{2} g_{\mu\nu} R + \Lambda g_{\mu\nu} = T_{\mu\nu}, \quad (3)$$

$$D_\mu F^{\mu\nu} = 0, \quad (4)$$

where

$$T_{\mu\nu} = \frac{1}{2} \text{Tr} [F_{\mu\gamma} F_\nu{}^\gamma] - \frac{1}{8} g_{\mu\nu} \text{Tr} [F_{\gamma\rho} F^{\gamma\rho}]. \quad (5)$$

Here we define the gauge covariant derivative as

$$D_\mu = \nabla_\mu + g_{\text{YM}} [A_\mu, \cdot]. \quad (6)$$

In explicit Lie index form, equation (4) is

$$D_\mu F^{\alpha\mu\nu} = \nabla_\mu F^{\alpha\mu\nu} + g_{\text{YM}} \epsilon^{abc} A_\mu^b F^{c\mu\nu} = 0. \quad (7)$$

In order to solve the equations of motion, we adopt the following radial direction (labelled coordinate z) field ansätze for the gauge field

$$A = A_\mu^a \tau^a dx^\mu = A_t^3 \tau^3 dt + A_x^1 \tau^1 dx = \phi(z) \tau^3 dt + \omega(z) \tau^1 dx, \quad (8)$$

and also the metric

$$ds^2 = \frac{1}{z^2} \left(-f(z) e^{-\chi(z)} dt^2 + \frac{1}{f(z)} dz^2 + h(z)^2 dx^2 + \frac{1}{h(z)^2} dy^2 \right). \quad (9)$$

Inserting these ansätze into equations (3) and (4) produces five individual equations of motion for the fields

$$\phi'' = \frac{\omega^2 \phi g_{\text{YM}}^2}{f h^2} - \frac{\chi' \phi'}{2} \quad (10)$$

$$\omega'' = -\frac{e^\chi \omega \phi^2 g_{\text{YM}}^2}{f^2} - \frac{f' \omega'}{f} + \frac{2h' \omega'}{h} + \frac{\chi' \omega'}{2} \quad (11)$$

$$h'' = \frac{e^\chi \omega^2 z^2 \phi^2 g_{\text{YM}}^2}{8 f^2 h} - \frac{f' h'}{f} + \frac{h' \chi'}{2} + \frac{2h'}{z} + \frac{(h')^2}{h} - \frac{z^2 (\omega')^2}{8h} \quad (12)$$

$$f' = \frac{e^\chi \omega^2 z^3 \phi^2 g_{\text{YM}}^2}{8 f h^2} + \frac{f z^3 (\omega')^2}{8 h^2} + \frac{f z (h')^2}{h^2} + \frac{3f}{z} - \frac{3}{L^2 z} + \frac{1}{8} e^\chi z^3 (\phi')^2 \quad (13)$$

$$\chi' = \frac{e^\chi \omega^2 z^3 \phi^2 g_{\text{YM}}^2}{8 f^2 h^2} + \frac{f'}{f} + \frac{3}{f L^2 z} - \frac{e^\chi z^3 (\phi')^2}{8 f} + \frac{z^3 (\omega')^2}{8 h^2} + \frac{z (h')^2}{h^2} - \frac{3}{z} \quad (14)$$

A non-trivial $\omega(z)$ profile is responsible for introducing the condensate, $\langle J_1^x \rangle$, to the model since it breaks the $U(1)$ subgroup symmetry associated to rotations around τ^3 . In other words, a non-zero $\omega(z)$ picks out the x direction as special and breaks the rotational symmetry in the $x-y$ plane. Naturally, the metric function $h(z)$ accounts for this symmetry breaking in the dual description. The chemical potential is associated with the $U(1)$ symmetry generated by τ^3 . $\phi(z)$ can be thought as the field dual to the chemical potential, appearing as the field charged under this $U(1)$ symmetry [8, 12, 13].

2.2 Boundary conditions

The equations of motion using this ansatz enjoy the following scaling symmetries

$$L \rightarrow \alpha_1 L, \quad f \rightarrow \frac{1}{\alpha_1^2} f, \quad g_{\text{YM}} \rightarrow \frac{1}{\alpha_1} g_{\text{YM}}, \quad e^\chi \rightarrow \frac{1}{\alpha_1^2} e^\chi. \quad (15a)$$

$$z \rightarrow \alpha_3 z, \quad \omega \rightarrow \frac{1}{\alpha_3} \omega, \quad \phi \rightarrow \frac{1}{\alpha_3} \phi. \quad (15b)$$

$$e^\chi \rightarrow \alpha_2^2 e^\chi, \quad \phi \rightarrow \frac{1}{\alpha_2} \phi. \quad (15c)$$

$$\omega \rightarrow \alpha_4 \omega, \quad h \rightarrow \alpha_4 h. \quad (15d)$$

The symmetries (15a) and (15b) allow us to take $z_h = L = 1$. The others also allow us to scale the χ and h fields such that they take their necessary boundary values: $\chi(z=0) = 0$ and

$h(z=0) = 1$. At the boundary we return to AdS spacetime (i.e. we have an asymptotically AdS bulk spacetime) which defines these conditions.

The procedure of numerically obtaining the field solutions from the equations of motion begins by producing series expansions of the fields at the horizon, $z = z_h = 1$, and at the UV boundary, $z = 0$. To be precise we only integrate up to a small cut-off value of z for the UV solutions, denoted as ϵ . Analogously we integrate to $z = 1 - \delta$ at the horizon, for small δ . The horizon series takes the following form

$$\begin{aligned}
f &= f_{h1}(z - z_h) + f_{h2}(z - z_h)^2 + \dots \\
\chi &= \chi_{h0} + \chi_{h1}(z - z_h) + \chi_{h2}(z - z_h)^2 + \dots \\
h &= h_{h0} + h_{h2}(z - z_h)^2 + \dots \\
\omega &= \omega_{h0} + \omega_{h2}(z - z_h)^2 + \omega_{h3}(z - z_h)^3 + \dots \\
\phi &= \phi_{h1}(z - z_h) + \phi_{h2}(z - z_h)^2 + \dots
\end{aligned} \tag{16}$$

Here f vanishes at $z = z_h$ by definition of the black hole event horizon, as does ϕ to ensure we have a finite norm of the gauge field strength squared. Substituting these series solutions into the equations of motion and solving order by order, the field functions are completely determined by four parameters at the horizon: ϕ_{h1} , ω_{h0} , h_{h0} , χ_{h0} . Using symmetry (15c), we choose $\chi_{h0} = 1$ throughout and rescale the necessary quantities when required, to ensure $\chi(z=0) = 0$ i.e. we set $\alpha_2 = e^{-\chi_{b0}/2}$ with χ_{b0} defined below in (17b). Repeating the same idea for the UV boundary expansion around $z = 0$, we find

$$f = 1 + f_{b3}z^3 + \mathcal{O}(z^4) \tag{17a}$$

$$\chi = \chi_{b0} + \mathcal{O}(z^4) \tag{17b}$$

$$h = h_{b0} + h_{b3}z^3 + \mathcal{O}(z^4) \tag{17c}$$

$$\omega = \omega_{b0} + \omega_{b1}z + \mathcal{O}(z^2) \tag{17d}$$

$$\phi = \phi_{b0} + \phi_{b1}z + \mathcal{O}(z^2) \tag{17e}$$

All higher order terms in z have coefficients that are constructed from the eight UV coefficient parameters listed in equations (17a)-(17e).

With the χ scaling symmetry allowing us to set $\chi_{h0} = 1$, we now look to set the horizon parameters ϕ_{h1} and h_{h0} such that we are left with a one-dimensional parameter space of solutions to explore, those being controlled by ω_{h0} . This requires two additional conditions. First, we require a vanishing source of the ω field, and in the chosen quantisation provided by the AdS/CFT correspondence, this corresponds to $\omega_{b0} = 0$ from the UV expansion. The correspondence also implies that the expectation value of the dual operator is identified as $\langle J_1^x \rangle = \omega_{b1}$. This is our condensate. Secondly, since we return to AdS spacetime at the boundary cut-off, we require that the anisotropy function $h(z)$ become unity there⁴. These two conditions serve as shooting parameters and root finding algorithms in Mathematica [33] for example, readily produce solutions. Additionally, the AdS/CFT dictionary states that the chemical potential, μ , and charge density, ρ , are identified with coefficients of the ϕ UV expansion such that $\mu = \phi_{b0}$, $\rho = \phi_{b1}$.

To establish where the condensate becomes non-trivial, the temperature must be defined. This is the Hawking temperature of the black hole described by equation (9) and can be

⁴In our numerical practice, we make use of the χ symmetry equation but not the h symmetry equation, instead choosing to “shoot” for the h function’s boundary value.

obtained through periodicity arguments of the metric's Euclidean signature

$$T = \left. \frac{|f'(z)|e^{-\chi(z)/2}}{4\pi} \right|_{z=z_h}. \quad (18)$$

Using the horizon expansion, this can be explicitly written as⁵

$$T = \frac{e^{-\frac{\chi_{h0}}{2}} \left(z_h^4 e^{\chi_{h0}} \phi_{h1}^2 - \frac{24}{L^2} \right)}{32\pi z_h}. \quad (19)$$

Overall, the model is simply determined by two parameters: T/μ , the dimensionless temperature, and g_{YM} , the coupling parameter of the matter fields. Having introduced the general method of acquiring solutions based on the boundary conditions, the following sections proceed to analyse the function content of said solutions, starting with the exterior of the black hole.

3 Thermodynamics

3.1 Phase transitions

Before exploring the interior, the core features of the black hole exterior are studied. We begin by presenting the field behaviour between the UV boundary, $z = 0$, and horizon, $z = z_h = 1$, at two different temperatures: one close to critical temperature shown in Figure 1 and one far away shown in Figure 2, both for $g_{\text{YM}} = 1$ (analysis shows that this coupling value permits typical normal-to-superconducting transitions).

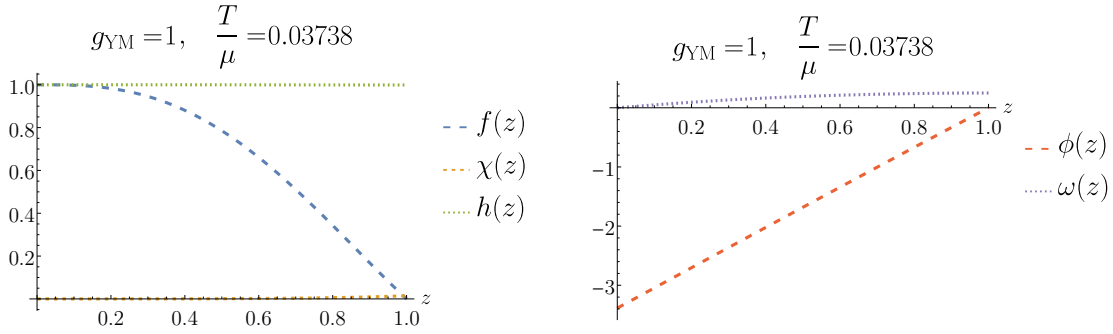


Figure 1: Plots of the matter and metric functions, for $T/\mu = 0.03738$ and $g_{\text{YM}} = 1$. The functions take on a simplified form close to critical temperature $T_c/\mu \approx 0.03748$. $\phi(z)$ becomes approximately linear, $\chi(z) \approx 0$ and $h(z) \approx 1$, while $\omega(z)$ is small and $f(z)$ has polynomial behaviour. Naturally when the temperature is raised above its critical value, the phase changes from superconducting to normal and the Reissner-Nordström geometry is recovered.

At both temperatures chosen, the functions achieve their correct forms at the horizon and UV boundaries: $\phi(z_h) = f(z_h) = 0$, while $h(0) = 1$, $\chi(0) = 0$ and $f(0) = 1$. Analytic temperatures for the $SU(2)$ model exist [34] and for these parameter choices the critical temperature is $T_c/\mu \approx 0.03748$. It therefore makes sense that Figure 1 exhibits such a form. Approaching critical temperature is essentially approaching normal phase where the

⁵This can be also be achieved directly using $T = \kappa/2\pi$ where κ is the surface gravity defined as $\kappa^2 = -\frac{1}{2}\nabla^\mu \xi^\nu \nabla_\mu \xi_\nu$ and ξ is the Killing vector.

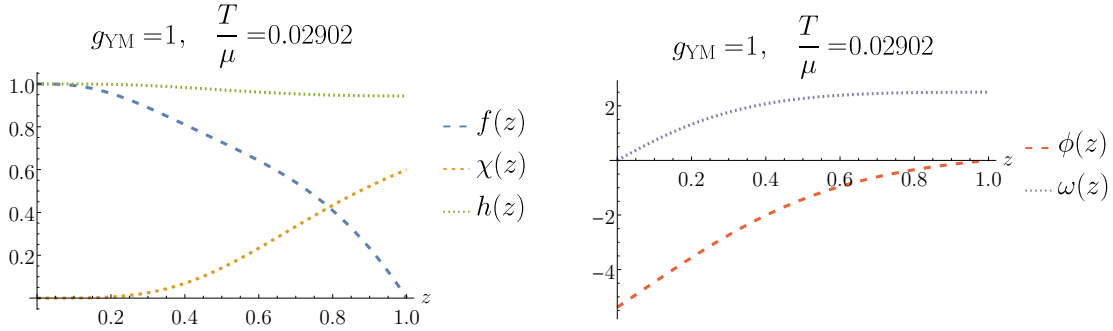


Figure 2: Plots of the matter and metric functions, for $T/\mu = 0.02902$ and $g_{\text{YM}} = 1$. The function behaviour far away from critical temperature (and within superconducting phase) is far more complicated. This is especially visible in the non-constant $h(z)$ and $\chi(z)$ and also in the larger value of $\omega(z)$ throughout the exterior.

condensate vanishes, $\omega(z) = 0$. When this occurs, we return to a Reissner-Nordström solution

$$\begin{aligned} \omega(z) = 0, \quad \phi(z) = \mu \left(1 - \frac{z}{z_h} \right), \\ \chi(z) = 0, \quad h(z) = 1, \quad f(z) = \frac{1}{L^2} - \frac{z^3}{L^2 z_h^3} - \frac{\mu^2 z^3}{8z_h} + \frac{\mu^2 z^4}{8z_h^2}. \end{aligned} \quad (20)$$

As expected the functions close to critical temperature of Figure 1 are converging to these solutions. This is clear by the non-linear behaviour of $f(z)$, the constant behaviours of $\chi(z)$ and $h(z)$, the linear behaviour of $\phi(z)$, and the diminishing value of $\omega(z)$ throughout the exterior. As for the lower temperature seen in Figure 2 the behaviour becomes more complicated since the solution is in superconducting phase. Note that these plots feature the rescaled functions i.e. using symmetry (15c).

Having observed the solutions, we now study the phase transitions for four choices of g_{YM} . The main feature found is the existence of a critical g_{YM} at which the phase transition changes from first to second order. This behaviour has appeared in [12, 35] where models of different dimension and Lagrangian⁶ were studied respectively⁷. Plots of the condensate vs. temperature are made in Figure 3 for the four g_{YM} values: $3/5$, 1 , $3/2$, 2 . Since $g_{\text{YM}} = 3/5$ appears multivalued and $g_{\text{YM}} = 1$ does not, the critical value should obey $3/5 < g_{\text{YM}}^c < 1$ and upon inspection we indeed find $g_{\text{YM}}^c = 0.8075 \pm 0.0025$.

⁶This model [35] can actually be identified with the present model under specific selection of fields/parameters, see appendix A of [30].

⁷Note that first order transitions were not found in [13], however, this was specifically due to the parameter range the authors chose to study: a range in which their g_{YM} values were greater than where we found first order transitions.

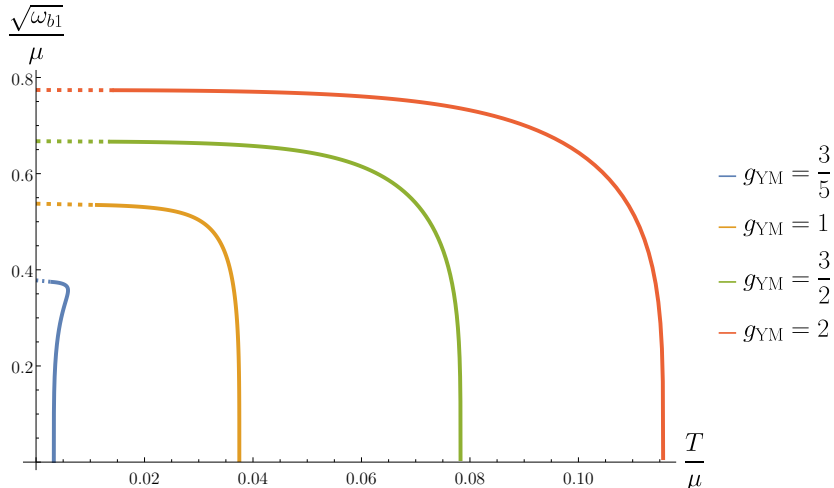


Figure 3: Phase diagrams for the four values of g_{YM} considered. The $g_{\text{YM}} = 1, 3/2$ and 2 curves all exhibit similar behaviour, while the $g_{\text{YM}} = 3/5$ curve becomes multi-valued between certain temperatures. This indicates that a critical value, g_{YM}^c , exists and from inspection is $g_{\text{YM}}^c = 0.8075 \pm 0.0025$. Below g_{YM}^c there are first order phase transitions, whilst above g_{YM}^c there will be second order transitions. This can be confirmed by studying the grand potential and entropy. The dashed part of the curves represent extrapolation of the data to reach zero temperature.

3.2 Grand potential and entropy analysis

To better understand the type of phase transition we see at these g_{YM} , the grand potential Ω , is calculated via the Euclidean action. The method outline is as follows. There are two solutions to the model which may be studied. The first is for normal phase where there is zero condensate, $\langle J_1^x \rangle = 0$. This corresponds to the Reissner-Nordström solution seen in (20). The second is for condensed phase where there is non-zero condensate $\langle J_1^x \rangle \neq 0$, based on the results of our full numerics. By generating Ω for both of these solutions, we can see which is physically favourable by identifying which takes the smaller value. Additionally the black hole entropy, S , is also calculated to help visualise the phase transition [12].

The grand potential, Ω , is simply the Euclidean action, I^E , multiplied by the temperature. In order to produce a well defined Dirichlet boundary problem for calculating the Euclidean action, we must include the standard Gibbons-Hawking boundary term, while to handle the divergences from both the bulk and boundary terms, a counter term must also be added. Hence, the total Euclidean action takes the form

$$I_{\text{total}}^E = \underbrace{- \int d^4x \sqrt{-g} \mathcal{L}}_{I_{\text{bulk}}^E} - \underbrace{\frac{2}{\kappa_{(4)}^2} \int d^3x \sqrt{-\gamma} \mathcal{K}}_{I_{\text{GH}}^E} - \underbrace{\frac{4}{\kappa_{(4)}^2} \int d^3x \sqrt{-\gamma}}_{I_{\text{ct}}^E}, \quad (21)$$

where $I_{\text{bulk}}^E, I_{\text{GH}}^E$ and I_{ct}^E are the Euclidean bulk, Gibbons-Hawking and counter terms respectively. We define γ_{ij} as the induced boundary metric on a fixed z hypersurface, z_b , and the determinant of γ_{ij} is denoted γ . Also, \mathcal{K} is the trace of the extrinsic curvature, defined as $\mathcal{K} = \gamma^{ij} K_{ji}$ where K_{ij} is the extrinsic curvature (second fundamental form).

Beginning with the bulk term, we may write it as

$$I_{\text{bulk}}^E = - \int d^4x \sqrt{-g} \frac{1}{\kappa_{(4)}^2} \left[R - 2\Lambda - \frac{1}{4} \text{Tr} [F_{\mu\nu} F^{\mu\nu}] \right] = -\beta V \int dz \sqrt{-g} \mathcal{L}, \quad (22)$$

with the d^4x now replacing $d^{3+1}x$ having adopted Euclidean signature with time coordinate, t_E . Creating the Euclidean action requires that $t_E \sim t_E + i\beta$ where β is the inverse temperature $T = 1/\beta$. In this case, integrating over the Euclidean time direction is integrating over the thermal circle. Since the Lagrangian is independent of t_E then the integration simply produces a factor of $\int dt_E = \beta$. Similarly, the Lagrangian is independent of x, y and so $\int dx dy = V$ is chosen to represent the volume of the two dimensional (x, y) -space.

To evaluate the integral, it is useful to note that the yy component of the Einstein tensor, $G_{\mu\nu} = R_{\mu\nu} - \frac{1}{2}g_{\mu\nu}R$, has a simple relationship with the Lagrangian \mathcal{L} [13]

$$G^y{}_y = \frac{1}{2} \left(\kappa_{(4)}^2 \mathcal{L} - R \right). \quad (23)$$

This connection allows us to describe \mathcal{L} purely in terms of metric functions⁸

$$\mathcal{L} = \frac{2}{\kappa_{(4)}^2} \left[G^\mu{}_\mu - (g^{tt}G_{tt} + g^{zz}G_{zz} + g^{xx}G_{xx}) \right] + \frac{R}{\kappa_{(4)}^2}. \quad (24)$$

where $G^\mu{}_\mu = g^{\mu\nu}G_{\nu\mu}$. Using our ansatz of the fields, one can then cast the Lagrangian above as

$$\mathcal{L} = \frac{z^4}{\kappa_{(4)}^2 e^{-\chi/2}} \left[\frac{2f e^{-\chi/2}}{z^3 h} (zh)' \right]'. \quad (25)$$

where α' denotes $d\alpha/dz$. The integral of (22) simplifies since the pre-factor of the total derivative in \mathcal{L} is simply the determinant of the metric. Therefore

$$I_{\text{bulk}}^E = -\beta V \int dz \sqrt{-g} \mathcal{L} \quad (26)$$

$$= -\frac{\beta V}{\kappa_{(4)}^2} \int dz \frac{e^{-\chi/2}}{z^4} \frac{z^4}{e^{-\chi/2}} \left[\frac{2f e^{-\chi/2}}{z^3 h} (zh)' \right]' \quad (27)$$

$$= -\frac{\beta V}{\kappa_{(4)}^2} \left[\frac{2f e^{-\chi/2}}{z^3 h} (zh)' \right] \Big|_{z=z_b}, \quad (28)$$

where we evaluate the bulk Euclidean action at $z = z_b$ which is taken as the boundary of space. After adding the GH term and finally the counterterm, this regulated hypersurface will be removed by taking $z_b \rightarrow 0$. Moving onto the GH term

$$I_{\text{GH}}^E = -\frac{2}{\kappa_{(4)}^2} \int d^3x \sqrt{-\gamma} \mathcal{K} = -\frac{\beta V}{\kappa_{(4)}^2} \frac{e^{-\chi/2}}{z^3} (zf' - f(6 + z\chi')) \Big|_{z=z_b}, \quad (29)$$

and finally the counterterm

$$I_{\text{ct}}^E = -\frac{4}{\kappa_{(4)}^2} \int d^3x \sqrt{-\gamma} = -\frac{\beta V}{\kappa_{(4)}^2} \frac{4e^{-\chi/2} \sqrt{f}}{z^3} \Big|_{z=z_b}. \quad (30)$$

Summing equations (28), (29) and (30) produces the total Euclidean action. Defining $\tilde{I}_{\text{total}}^E = \frac{1}{\beta} I_{\text{total}}^E$ for convenience, we have

$$\Omega = \lim_{z \rightarrow z_b} \tilde{I}_{\text{total}}^E = -\frac{V}{\kappa_{(4)}^2} \frac{e^{-\chi/2}}{z^3} \left[\frac{2f}{h} (zh)' + zf' - f(6 + z\chi') + 4\sqrt{f} \right] \Big|_{z=z_b}. \quad (31)$$

⁸Alternatively, one may substitute the equations of motion directly into the Lagrangian to remove second derivatives and achieve the same form as equation (25).

In order to evaluate Ω , we must take z_b as some small cut off. This permits the insertion of the UV boundary expansions into (31), and afterwards the regulator can be removed by taking $z_b \rightarrow 0$. Doing so results in the final expression

$$\Omega = -\frac{V}{\kappa_{(4)}^2}(f_{b3} + 6h_{b3}). \quad (32)$$

A natural check of this quantity as well as the consistency of conformality on the boundary, comes from analysis of the boundary stress energy tensor [36, 37]. The stress energy tensor for the present model is defined as

$$\langle T_{ij} \rangle = \lim_{z \rightarrow z_b} \frac{2}{\sqrt{\gamma}} \frac{\delta \tilde{I}_{\text{total}}^E}{\delta \gamma^{ij}} = -\frac{2V}{\kappa_{(4)}^2} \lim_{z \rightarrow z_b} \frac{1}{z} (K_{ij} - \mathcal{K} \gamma_{ij} - 2\gamma_{ij}). \quad (33)$$

Again, using the ansätze and substituting in the UV boundary expansion, we obtain the three stress tensor boundary components

$$\langle T_{tt} \rangle = \frac{V}{\kappa_{(4)}^2} (2f_{b3}), \quad (34)$$

$$\langle T_{xx} \rangle = \frac{V}{\kappa_{(4)}^2} (f_{b3} - 6h_{b3}), \quad (35)$$

$$\langle T_{yy} \rangle = \frac{V}{\kappa_{(4)}^2} (f_{b3} + 6h_{b3}), \quad (36)$$

where we have taken the hypersurface $z_b \rightarrow 0$. We find that $-\langle T_{tt} \rangle + \langle T_{xx} \rangle + \langle T_{yy} \rangle = 0$, which states that the stress energy tensor is indeed traceless (when in Lorentzian signature), as it should be for a conformally invariant theory on the boundary. We also find that $\Omega = -\langle T_{yy} \rangle$. In the normal phase case⁹, see (20), we must have $h(z) = 1$ and as such h_{b3} becomes zero (since $h_{b0} = 1$ automatically) while function $f(z)$ identifies the z^3 coefficient as $f_{b3} = -\left(\frac{1}{z_h^3} + \frac{\mu^2}{8z_h}\right)$, when setting $L = 1$. Additionally, $\phi_{h1} = -\mu/z_h$ by virtue of its functional solution $\phi(z) = \mu(1 - \frac{z}{z_h})$. The entropy calculated is the Bekenstein-Hawking entropy, S , given by the formula

$$S = \frac{2\pi A_h}{\kappa_{(4)}^2} = \frac{2\pi V}{z_h^2 \kappa_{(4)}^2}. \quad (37)$$

To produce meaningful values of both S and Ω , we make the quantities dimensionless by introducing the necessary factors of μ . Plots of the grand potential and entropy for both normal (blue curve) and condensing (red, dashed curve) phases at each g_{YM} are presented in Figures 4 to 11. Here we confirm the nature of the phase transitions at each g_{YM} . Figures 4 and 5 detail Ω and S for $g_{\text{YM}} = 3/5$ and show different behaviour to the other g_{YM} . Starting with Ω at higher temperatures (far right side of the plot), the blue normal curve starts as the only solution, until approximately $T/\mu \approx 0.0059$ after which the condensed phase curve emerges, and exhibits a two-branch ‘‘swallow tail’’ form. The blue curve continues to be the smaller-valued, preferred Ω until a critical temperature where it intersects the red condensed phase curve, after which the condensed curve becomes preferable. This intersection

⁹Owing to the simplification in functions, normal phase and the thermodynamic quantities are all determined by the parameter $\phi_{h1} = -\mu/z_h$. Hence, selecting a range of values of ϕ_{h1} or μ lets us acquire Ω .

is continuous, but not differentiable, which indicates a first order phase transition. This outcome is further confirmed by the entropy plot in Figure 5. At $T = T_c$ clearly the entropy is not continuous between normal and condensed phases, as there is a jump between the blue curve and lowest red curve branch. As for the larger g_{YM} values we chose to study, they all display second order phase transition behaviour. In Figures 6, 8 and 10, Ω is both continuous and differentiable, while S is continuous but not differentiable at $T = T_c$: the defining characteristics of second order phase transitions.

These results are in keeping with the previous literature, in particular Figures 10 and 11 show similar behaviour to the results of [13] (see their Figures 4 and 5)¹⁰. As for the identification of a critical g_{YM} , [12] initially showed that there exists a critical coupling value “ α_c ” (analogous to the reciprocal of g_{YM} in our work) in 5-dimensions where above α_c , one finds first order transitions and below they are second order. Similar results were found in [35] which used two parameters: scalar field mass and charge¹¹.

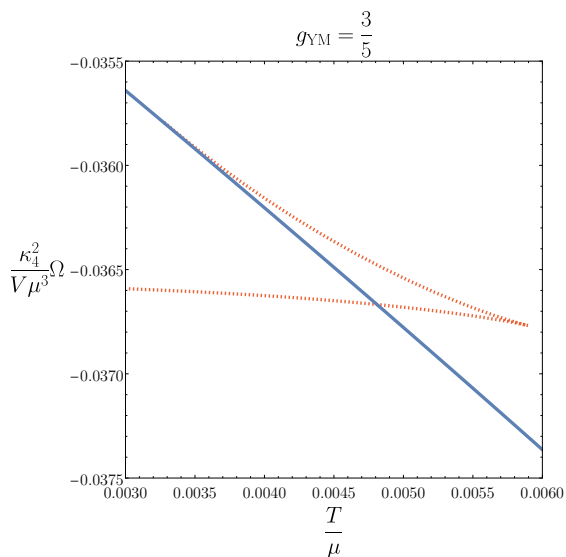


Figure 4: The grand potential Ω as a function of temperature for both normal (blue) and condensed (red, dashed) phase with $g_{\text{YM}} = 3/5$. The condensed phase curve exhibits swallow tail behaviour, and the intersection between it and the normal phase curve shows that Ω is continuous, but non-differentiable. This is characteristic of first order phase transition.

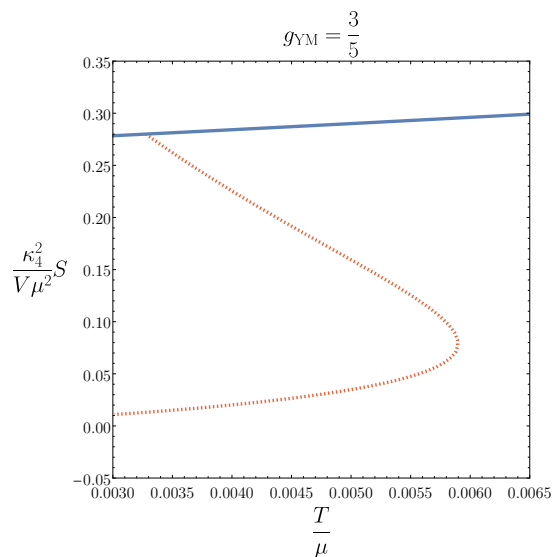


Figure 5: The entropy S as a function of temperature for both normal (blue) and condensed (red, dashed) phase with $g_{\text{YM}} = 3/5$. At $T = T_c$, the condensed curve is not continuous as following the normal curve down past $T = T_c$, there is discontinuous jump to the lower condensed curve branch. The behaviour exhibited in these plots is therefore that of first order phase transition.

¹⁰upon redefining the temperature by a factor of 1/2.

¹¹To our knowledge, the specific result of a critical g_{YM} in four dimensions is new.

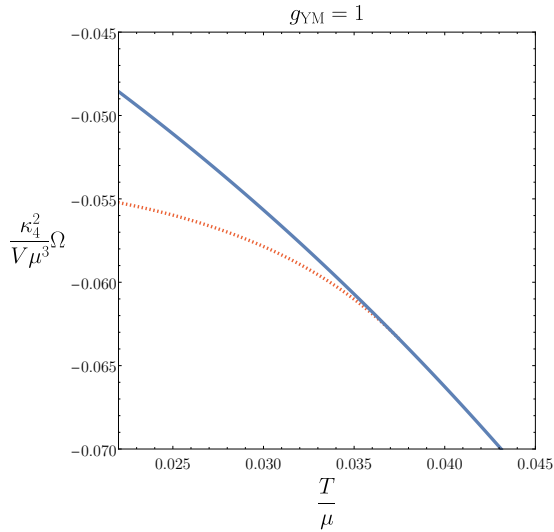


Figure 6: The grand potential Ω as a function of temperature for both normal and condensed phase with $g_{\text{YM}} = 1$. The red dashed curve (condensed phase, $\langle J_1^x \rangle \neq 0$) and the blue curve (normal phase, $\langle J_1^x \rangle = 0$) smoothly intersect showing that Ω is both continuous and differentiable.

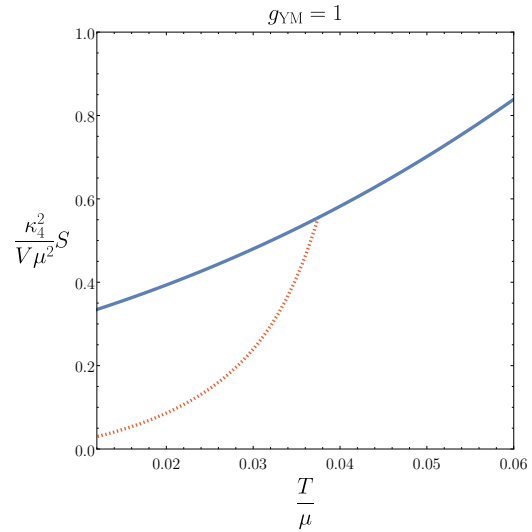


Figure 7: The entropy S as a function of temperature for both normal (blue) and condensed (red, dashed) phase with $g_{\text{YM}} = 1$. At $T = T_c$, the red curve is continuous but non-differentiable. The behaviour exhibited is therefore that of second order phase transition.

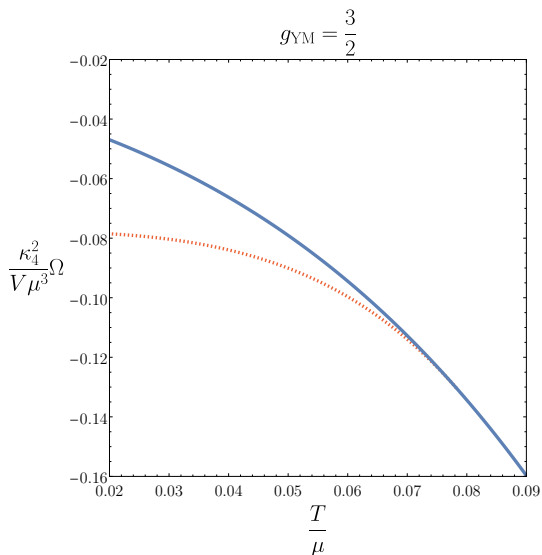


Figure 8: The grand potential Ω as a function of temperature for both normal and condensed phase with $g_{\text{YM}} = 3/2$. The red dashed curve (condensed phase, $\langle J_1^x \rangle \neq 0$) and the blue curve (normal phase, $\langle J_1^x \rangle = 0$) smoothly intersect showing that Ω is both continuous and differentiable.

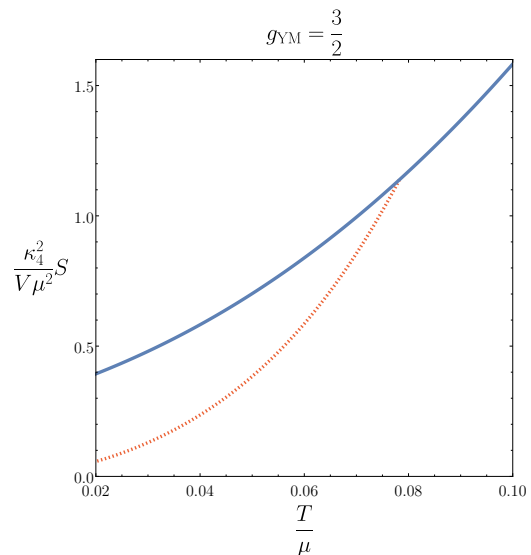


Figure 9: The entropy S as a function of temperature for both normal (blue) and condensed (red, dashed) phase with $g_{\text{YM}} = 3/2$. At $T = T_c$, the red curve is continuous but non-differentiable. The behaviour exhibited is therefore that of second order phase transition.

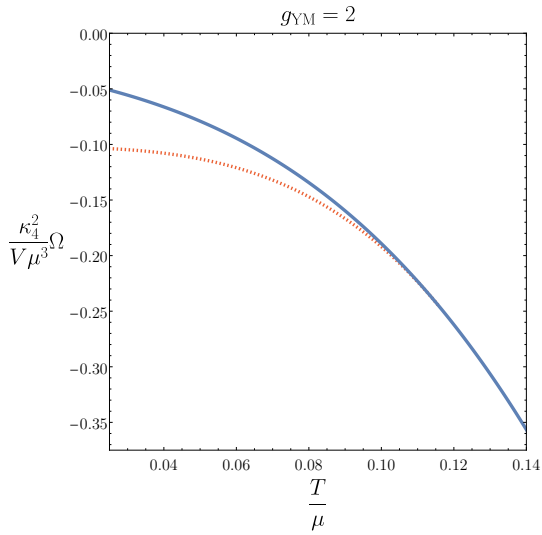


Figure 10: The grand potential Ω as a function of temperature for both normal and condensed phase with $g_{\text{YM}} = 2$. The red dashed curve (condensed phase, $\langle J_1^x \rangle \neq 0$) and the blue curve (normal phase, $\langle J_1^x \rangle = 0$) smoothly intersect showing that Ω is both continuous and differentiable.

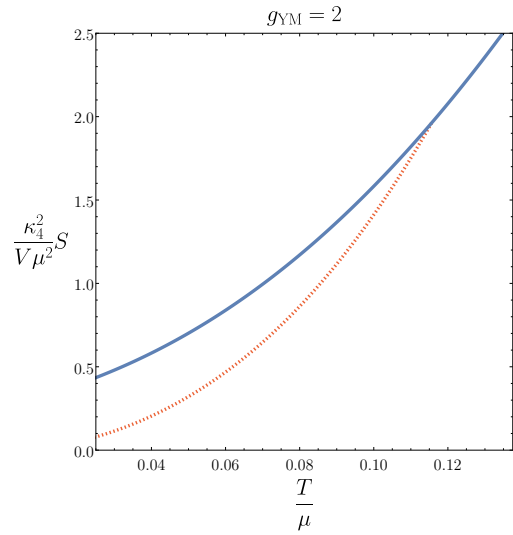


Figure 11: The entropy S as a function of temperature for both normal (blue) and condensed phase (red, dashed) with $g_{\text{YM}} = 2$. At $T = T_c$, the red curve is continuous but non-differentiable. The behaviour exhibited is therefore that of second order phase transition.

4 Black hole interior

By virtue of the numerical solutions to the equations of motion, we can study the black hole interior by extending the bulk radial coordinate range from $z = z_h = 1$ toward $z \rightarrow \infty$. The black hole interior has previously been investigated, for example [38, 39]. However, the emergence of Kasner geometry in the interior, in the context of holographic superconductors, was initially identified in [14, 15, 16], where the typical scalar field condensation was utilised. Following this, the interior of vector condensate holographic superconductors appeared in [30] where numerous Kasner universes were found. The analysis of the interior presented in this section further explores the ω_{h0} parameter space. The ω_{h0} values correspond to the coefficient of the horizon expansion in (16). Note that ω_{h0} is only a function of the temperature¹².

4.1 Josephson oscillations

We begin by providing some typical interior plots which demonstrate the common phenomena. Figures 12 and 13 introduce an initial view of the interior by plotting particular metric and condensate functions. Both plots extend over a small radial range $z \in (1, 50]$ and take $g_{YM} = 1$. Figure 12 depicts a low temperature $T/\mu = 0.02902$ where the metric functions take rather simple form. On the other hand, pushing closer to critical temperature, $T_c/\mu = 0.03748$, far more interesting phenomena emerge in Figure 13 for $T/\mu = 0.03738$. Firstly $\log g_{tt}$, begins to rapidly decline around $z \approx 1.5$ which is directly followed by rapid oscillations in $\omega(z)$ and $h(z)$. These are the Einstein-Rosen (ER) bridge collapse and Josephson oscillations¹³. Notably, the presence of the ER bridge collapse produces these first oscillations, and as will be seen shortly, further changes in the $\log g_{tt}$ function also indicate the presence of different Kasner universes. Interestingly, $h(z)$ has twice the frequency of $\omega(z)$. The reason for this can be traced back to analytic results coming from the simplified equations of motion [30].

¹² ω_{h0} is the last free horizon parameter once the boundary conditions are used. In this sense, it can be thought of as defining h_{h0} and ϕ_{h1} which in turn, define T/μ . In reference to section 2 we can therefore see our parameters as either $(T/\mu, g_{YM})$ or (ω_{h0}, g_{YM}) . We chose ω_{h0} instead of temperature out of numerical convenience.

¹³More specifically the Josephson oscillations are associated to the oscillations in $\omega(z)$ rather than $h(z)$, as this is the condensate's dual field.

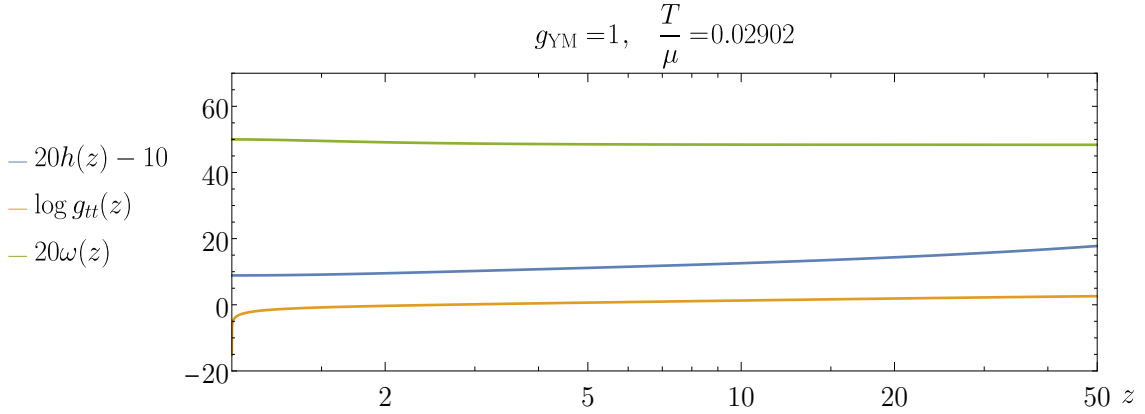


Figure 12: Low temperature plot of the black hole interior functions. The functions plotted $h(z)$, $\omega(z)$, $\log(g_{tt})$ exhibit tame behaviour in the early interior which is generally the case for lower temperatures.

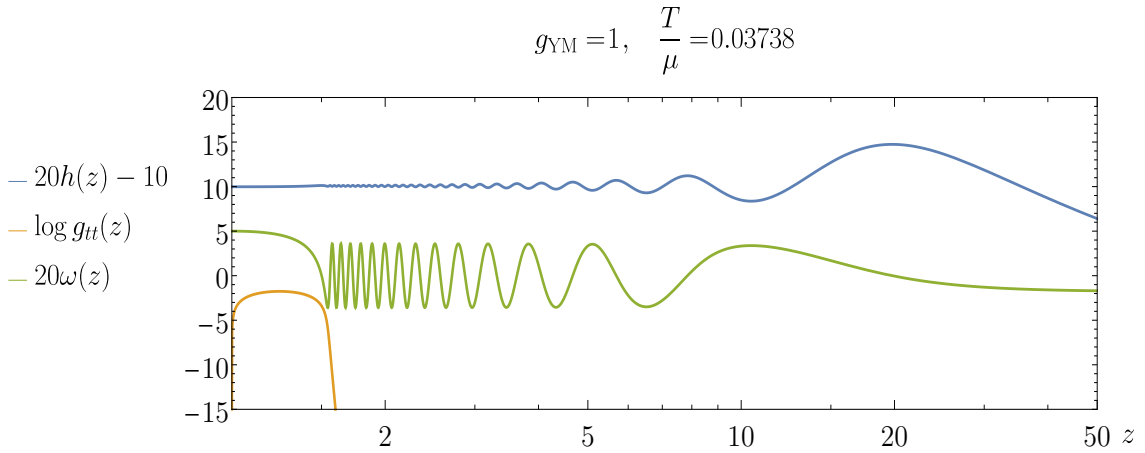


Figure 13: High temperature plot of the black hole interior functions. Far more interesting phenomena emerge for functions $h(z)$, $\omega(z)$, $\log(g_{tt})$, when close to critical temperature. Here we identify the Josephson oscillations of condensate function $\omega(z)$, while the large decrease in $\log(g_{tt})$ at $z \approx 1.5$ is known as the collapse of the Einstein-Rosen bridge.

4.2 Kasner regime

To discover the Kasner universes, we must explore a larger z -coordinate range. Just why these Kasner geometries appear in this regime can be understood from the full numerical solutions as well as from a simplified set of analytic solutions. These solutions are given below and the analysis of the interior and graphical representation of the alternations follows.

$$g_{\text{YM}} = 1, \quad \frac{T}{\mu} = 0.03348$$

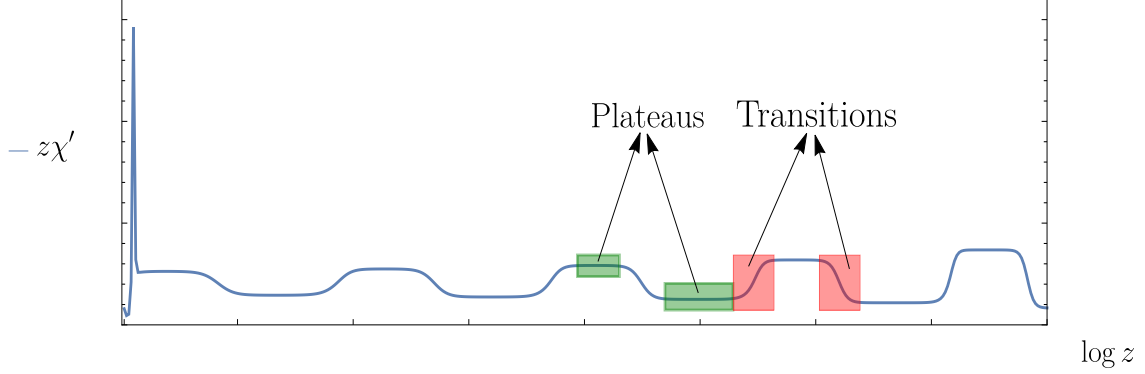


Figure 14: An example of the interior of the black hole demonstrating function $z\chi'$ for large z , at $g_{\text{YM}} = 1$ and $T/\mu = 0.03348$. On this data we see that up to $\log z = 400$, there are five oscillations in $z\chi'$. The different plateaus (two highlighted in green) of each oscillation correspond to a different n_h and thus different Kasner universes. The transitions (two highlighted in red) detail how neighbouring Kasner universes connect.

For the current model, by removing the terms which are negligible we arrive at the set of simplified EOM

$$\begin{aligned}
 f' &= \frac{3f}{z} + \frac{zf(h')^2}{h^2} \\
 \chi' &= \frac{2z(h')^2}{h^2} \\
 h'' &= \frac{2h'}{z} - \frac{f'h'}{f} + \frac{(h')^2}{h} + \frac{h'\chi'}{2} \\
 \phi'' &= -\frac{\phi'\chi'}{2} \\
 \omega'' &= -\frac{f'\omega'}{f} + \frac{2h'\omega'}{h} + \frac{\chi'\omega'}{2}
 \end{aligned} \tag{38}$$

which have the resulting analytic solutions

$$\begin{aligned}
 f(z) &\approx f_0 z^{3+n_h^2}, \quad \chi(z) \approx 2n_h^2 \log(z) + \chi_0, \quad h(z) \approx h_0 z^{n_h}, \\
 \omega(z) &\approx \frac{z^{2(n_h-1)}}{2(n_h-1)} \omega_1 + \omega_0, \quad \phi(z) \approx \frac{z^{1-n_h^2}}{1-n_h^2} \phi_1 + \phi_0,
 \end{aligned} \tag{39}$$

where $f_0, \chi_0, h_0, \omega_1, \omega_0, \phi_1, \phi_0$ and n_h are all constants. The simplicity of these solutions reveals the Kasner geometry previous mentioned. By taking proper time to be $\tau = \tau_0 z^{-\frac{1}{2}(3+n_h^2)}$, along with the simplified solutions (39), the metric adopts the following form

$$ds^2 = -d\tau^2 + c_t \tau^{2p_t} dt^2 + c_x \tau^{2p_x} dx^2 + c_y \tau^{2p_y} dy^2, \tag{40}$$

where $\tau_0, c_t, c_x, c_y, p_t, p_x$ and p_y are constants¹⁴. This is a Kasner universe and the connection between the Kasner exponents, p_t, p_x, p_y , and n_h is:

$$p_t = \frac{(n_h^2 - 1)}{3 + n_h^2}, \quad p_x = \frac{2(1 - n_h)}{3 + n_h^2}, \quad p_y = \frac{2(n_h + 1)}{3 + n_h^2}. \tag{41}$$

¹⁴Suitable choice of τ_0 allows one to scale the $d\tau^2$ coefficient to -1.

One can indeed verify these exponents determine a Kasner universe since $\sum_{i=1}^3 p_i = \sum_{i=1}^3 p_i^2 = 1$ for $i = 1, 2, 3 = t, x, y$. To clearly see the alternations between different Kasner universes, Figure 14 plots $z\chi'$ from the horizon to a large radial z value. This function presents a way to visually interpret the different Kasner universes that appear, as it either takes on different constant values for a given z which we refer to as “plateaus” (the blocks in green), or it transitions between them (blocks in red). These plateaus’ constant values are $z\chi' = 2n_h^2$, which determines n_h and in turn defines the exponents (41). As will be seen in future figures, the transitions (see [16, 24]) inbetween are brought about by stationary points of the $\log g_{tt}$ function.

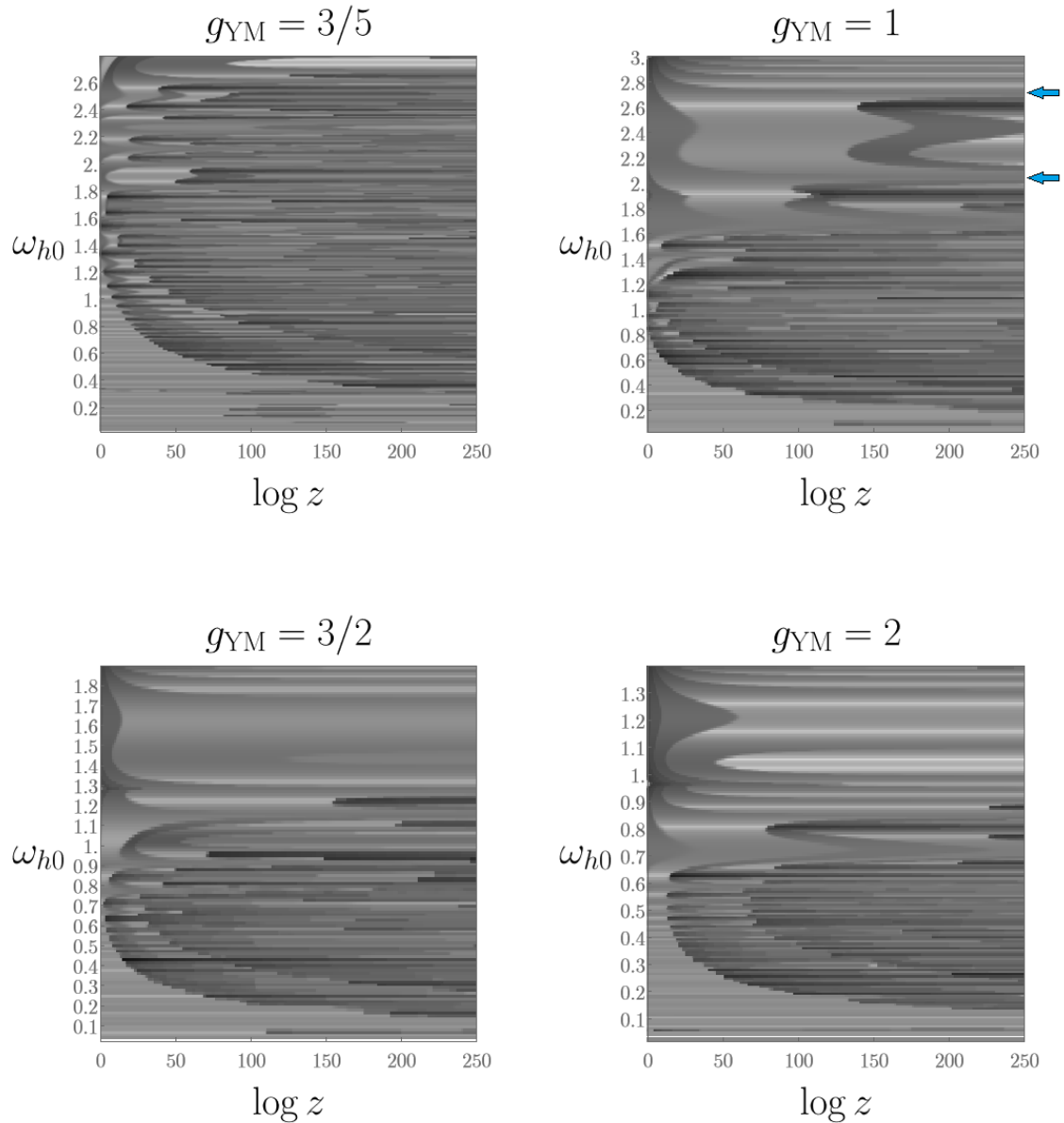


Figure 15: Density plots for function $z\chi'$ at the four values of g_{YM} : $3/5, 1, 3/2$ and 2 . The chaotic nature at small ω_{h0} (and correspondingly, high temperatures) is visible, while more structure arises at larger ω_{h0} choices. Particular values of ω_{h0} correspond to critical points, denoted by the blue arrows.

4.3 Near-oscillatory Kasner epoch

Firstly, to observe the general complicated behaviour in the interior as a function of temperature, Figure 15 provides density plots of the function $z\chi'$ for bulk radial coordinate $\log(z)$ (x-axis) vs. horizon parameter ω_{h0} (y-axis). Since choice of ω_{h0} defines ϕ_{h1} as well as the UV boundary values (μ, ρ e.t.c.) for a given solution via our shooting method, then choice of ω_{h0} essentially sets the temperature T/μ . Hence the parameter spaces of ω_{h0} and T/μ are somewhat interchangeable, but we will refer to ω_{h0} directly in most cases. The four plots for $g_{\text{YM}} = 3/5, 1, 3/2, 2$ all demonstrate complicated behaviour at small ω_{h0} (high temperature). For example, for $\omega_{h0} = (0.1, 1.1)$ in the $g_{\text{YM}} = 3/2$ plot, the density changes drastically so the various n_h values for each plateau do also. This behaviour spans a wider range of ω_{h0} in the smaller g_{YM} value plots¹⁵.

The key result of this paper is that while exploration of the parameter space yields generally complicated functions, there are values of the temperature where the functions become stable and almost oscillatory. To be more specific, the alternations between different Kasner epochs at these particular temperatures become far more regular.

As an example, take $\omega_{h0} = 2.05$ on the $g_{\text{YM}} = 1$ density plot of Figure 15. A change in density along this value indicates that we may observe many oscillations, hence prompts exploration around this value. The plots of $\log g_{tt}$ and $z\chi'$ with large radial range corresponding to this particular $\omega_{h0} = 2.05$ value, are given in Figures 16 and 17. Here we see the oscillatory nature more clearly, with numerous oscillations extending deep towards the black hole singularity, plotted up to $\log z = 40000$. The amplitude of oscillations in both figures increases as we approach larger z . Our numerics was shown to breakdown past these large- z values¹⁶. It is a natural question to pose whether fine tuning ω_{h0} can lead to an infinite number of oscillations that extend all the way to the singularity. The answer to this appears to be that we can approach this highly oscillatory behaviour and at some point the number of oscillations goes to infinity. This is indicated by the lower blue arrow in the $g_{\text{YM}} = 1$ plot, Figure 15. We aim to provide evidence of this by observing the relation between the wavelength of $\log g_{tt}$ vs. ω_{h0} , as well as the n_h Kasner parameter in the subsequent section.

¹⁵Note that these plots were generated with an averaging approach due to time constraints on the numeric calculations. In more detail, the numerical integration up to $\log z = 250$ for some ω_{h0} values was unable to complete in reasonable time. When this occurred, the $z\chi'$ value associated to this ω_{h0} was then filled in by taking an average of the $z\chi'$ values adjacent to it in the ω_{h0} parameter space.

¹⁶We thank Sean Hartnoll for correspondence on this matter.

$$g_{\text{YM}} = 1, \quad \frac{T}{\mu} = 0.03143$$

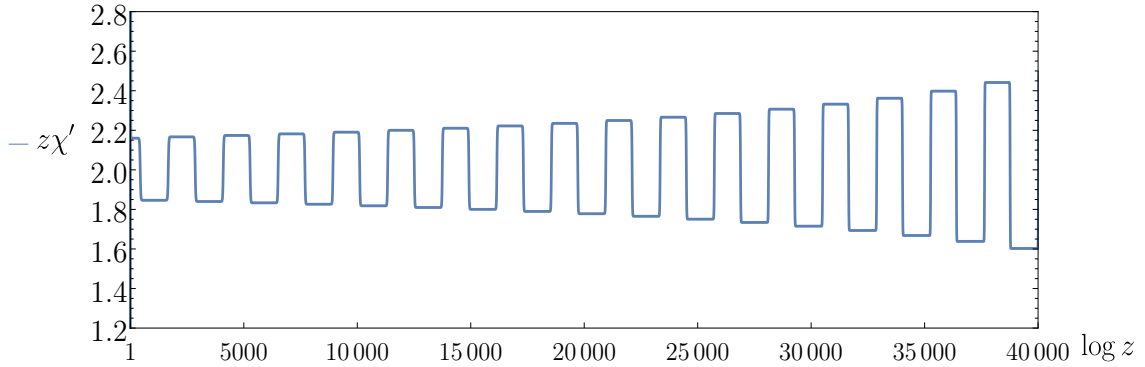


Figure 16: Large- z plot for function $z\chi'$ at $\omega_{h0} = 2.05$. The function demonstrates a large number of oscillations by virtue of the many plateaus. These plateau oscillations are centred around $z\chi' = 2$, which is the value that sets $n_h = 1$. The oscillation amplitude grows with z and at very large z the numerics becomes unstable.

$$g_{\text{YM}} = 1, \quad \frac{T}{\mu} = 0.03143$$

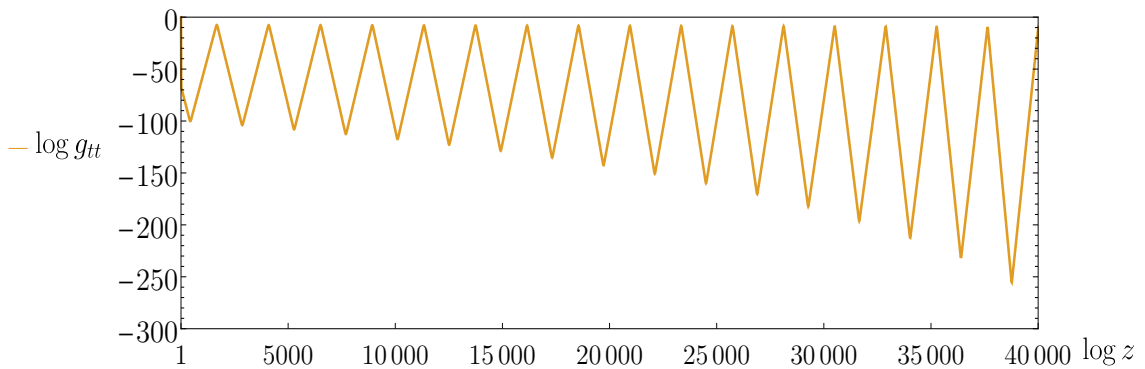


Figure 17: Large- z plot for function $\log g_{tt}$ at $\omega_{h0} = 2.05$. The function demonstrates a large number of oscillations. The oscillation amplitude grows with z .

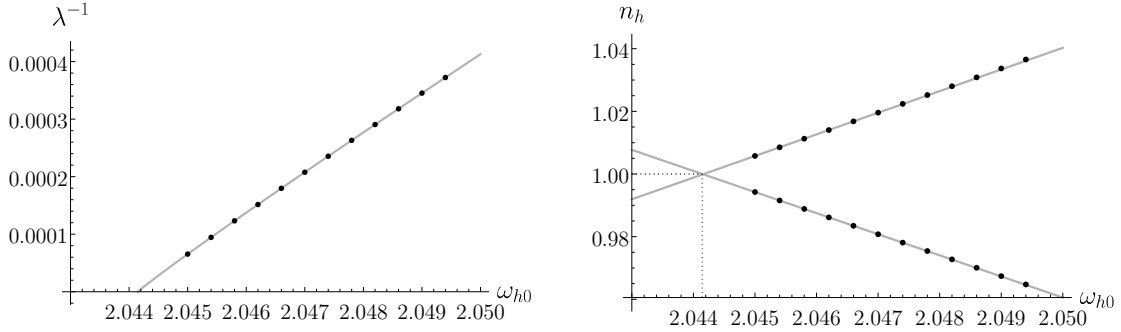


Figure 18: As seen in Figure 17, $\log g_{tt}(z)$ is periodic in $\log z$. The left plot demonstrates the reciprocal wavelength of $\log g_{tt}$ (labelled λ^{-1}) as a function of ω_{h0} . The data collected (black points) are well fitted to a simple power law model (grey curve), with exponent 0.96 ± 0.01 . The right plot displays n_h , see equation (39), as a function of ω_{h0} for the first two plateaus. The data for either of the plateaus are well fitted to a linear function.

Understanding how varying ω_{h0} can lead to a large number of Kasner epoch alternations can be achieved as follows. We calculate how the reciprocal wavelength of $\log g_{tt}$ (labelled λ^{-1}) changes upon varying ω_{h0} . The data range explored is from $\omega_{h0} = (2.045, 2.05)$ and the results are presented in left plot of Figure 18. As the figure shows, the data are in good agreement with the fitted model

$$\lambda^{-1} = a(\omega_{h0} - \omega_*)^b \quad (42)$$

with

$$a = 0.056 \pm 0.002, \quad b = 0.96 \pm 0.01, \quad \omega_* = 2.04415 \pm 0.00001. \quad (43)$$

At $\omega_{h0} = \omega_*$, the wavelength diverges. At this point we expect that the first plateau extends to infinity and $\log g_{tt} = \text{const.}$. The right plot of Figure 18 displays n_h as a function of ω_{h0} . The data are taken from the first two plateaus and a linear fit is applied. The fitted value of ω_* agrees with the value found from the λ^{-1} analysis. Similar fits on the other side of the critical point ($\omega_{h0} < \omega_*$) match the coefficients of equation (43).

The plot also indicates by the dashed curves that both $n_h \rightarrow 1$ as $\omega_{h0} \rightarrow \omega_*$. Note that $n_h = 1$ corresponds to a special Kasner geometry since from (41) we have $p_t = p_x = 0$ and $p_y = 1$. Plugging these p_i into (40) and finally making the coordinate transformation

$$\hat{\tau} = \sqrt{c_y} \tau \cosh(\sqrt{c_y} y) \quad \hat{y} = \sqrt{c_y} \tau \sinh(\sqrt{c_y} y), \quad (44)$$

we find that the metric, up to choice of constants c_i , is flat spacetime

$$ds^2|_{n_h=1} = -\frac{1}{c_y} d\hat{\tau}^2 + c_t dt^2 + c_x dx^2 + \frac{1}{c_y} d\hat{y}^2. \quad (45)$$

τ and y are the well known Rindler coordinates, however, instead of the time and radial z -direction, we transform the time and y -direction.

Ultimately the analysis tells us that at $\omega_{h0} = \omega_*$, we obtain flat geometry. Moving slightly away from this value leads to many oscillations between Kasner universes centred around the $n_h = 1$ value. The parameter space can be scanned and it is possible to find additional critical points. For example at $g_{\text{YM}} = 1$, $\omega_{h0} = 2.713$ the metric functions also exhibit multiple oscillations, see Figures 19 and 20. This ω_{h0} value corresponds to the upper blue arrow in the density plot of Figure 15.

$$g_{\text{YM}} = 1, \quad \frac{T}{\mu} = 0.02785$$

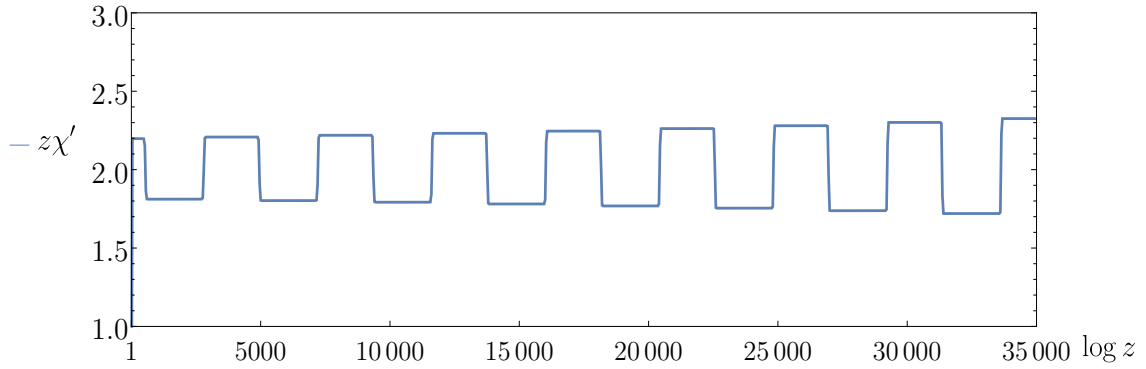


Figure 19: Large- z plot for $z\chi'$ at $\omega_{h0} = 2.713$. The function once again demonstrates a large number of oscillations at this ω_{h0} . The function is shown to oscillate around $z\chi' = 2$ or analogously $n_h = 1$.

$$g_{\text{YM}} = 1, \quad \frac{T}{\mu} = 0.02785$$

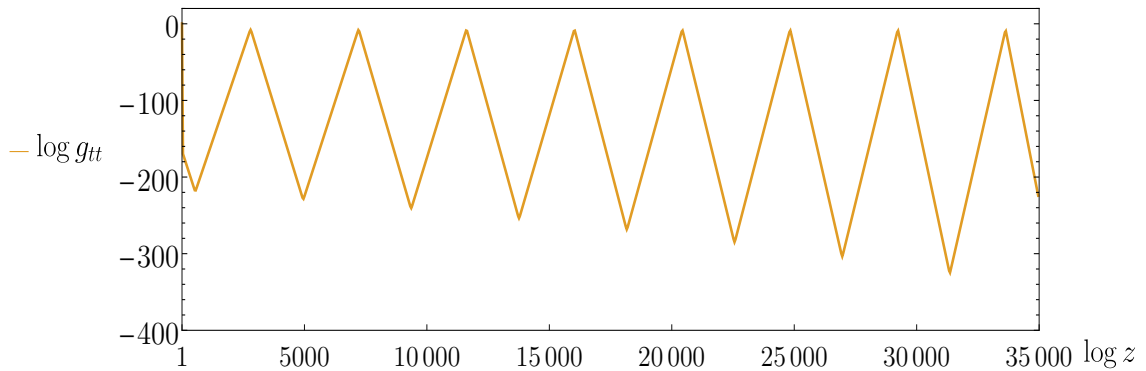


Figure 20: Large- z plot for $\log g_{tt}$ at $\omega_{h0} = 2.713$. The function demonstrates a large number of oscillations, with increasing amplitude.

5 Conclusion

In this paper we used a holographic p-wave superconductor to explore what lies beyond the black hole horizon. Beginning with the black hole exterior, our numerical results showed that phase transitions are dependent on the Yang-Mills coupling parameter g_{YM} with a critical value that separates first and second order phase transitions. The interior yielded further interesting results upon exploring the parameter space. At specific temperature values the geometry of the interior becomes flat. Approaching these temperature values a large number of Kasner universe alternations appear. It is possible that further investigation of the parameter space could yield other regions of interest.

Acknowledgements

We thank Pau Figueras, Damián Galante and Sean Hartnoll for useful discussions. LS is supported by an STFC quota studentship. DV is supported by the STFC Ernest Rutherford grant ST/P004334/1. No new data were generated or analysed during this study.

References

- [1] Juan Martin Maldacena. “The Large N limit of superconformal field theories and supergravity”. In: *Adv. Theor. Math. Phys.* 2 (1998), pp. 231–252. arXiv: [hep-th/9711200](#).
- [2] Edward Witten. “Anti-de Sitter space and holography”. In: *Adv. Theor. Math. Phys.* 2 (1998), pp. 253–291. arXiv: [hep-th/9802150](#).
- [3] S. S. Gubser, Igor R. Klebanov, and Alexander M. Polyakov. “Gauge theory correlators from noncritical string theory”. In: *Phys. Lett. B* 428 (1998), pp. 105–114. arXiv: [hep-th/9802109](#).
- [4] Steven S. Gubser. “Breaking an Abelian gauge symmetry near a black hole horizon”. In: *Phys. Rev. D* 78 (2008), p. 065034. arXiv: [0801.2977 \[hep-th\]](#).
- [5] Sean A. Hartnoll, Christopher P. Herzog, and Gary T. Horowitz. “Building a Holographic Superconductor”. In: *Phys. Rev. Lett.* 101 (2008), p. 031601. arXiv: [0803.3295 \[hep-th\]](#).
- [6] Sean A. Hartnoll, Christopher P. Herzog, and Gary T. Horowitz. “Holographic Superconductors”. In: *JHEP* 12 (2008), p. 015. arXiv: [0810.1563 \[hep-th\]](#).
- [7] Keun-Young Kim and Marika Taylor. “Holographic d-wave superconductors”. In: *JHEP* 08 (2013), p. 112. arXiv: [1304.6729 \[hep-th\]](#).
- [8] Steven S. Gubser and Silviu S. Pufu. “The Gravity dual of a p-wave superconductor”. In: *JHEP* 11 (2008), p. 033. arXiv: [0805.2960 \[hep-th\]](#).
- [9] Martin Ammon, Johanna Erdmenger, Matthias Kaminski, and Patrick Kerner. “Superconductivity from gauge/gravity duality with flavor”. In: *Phys. Lett. B* 680 (2009), pp. 516–520. arXiv: [0810.2316 \[hep-th\]](#).
- [10] Pallab Basu, Jianyang He, Anindya Mukherjee, and Hsien-Hang Shieh. “Superconductivity from D3/D7: Holographic Pion Superfluid”. In: *JHEP* 11 (2009), p. 070. arXiv: [0810.3970 \[hep-th\]](#).

- [11] Martin Ammon, Johanna Erdmenger, Matthias Kaminski, and Patrick Kerner. “Flavor Superconductivity from Gauge/Gravity Duality”. In: *JHEP* 10 (2009), p. 067. arXiv: 0903.1864 [hep-th].
- [12] Martin Ammon, Johanna Erdmenger, Viviane Grass, Patrick Kerner, and Andy O’Bannon. “On Holographic p-wave Superfluids with Back-reaction”. In: *Phys. Lett. B* 686 (2010), pp. 192–198. arXiv: 0912.3515 [hep-th].
- [13] Raul E. Arias and Ignacio Salazar Landea. “Backreacting p-wave Superconductors”. In: *JHEP* 01 (2013), p. 157. arXiv: 1210.6823 [hep-th].
- [14] Alexander Frenkel, Sean A. Hartnoll, Jorrit Kruthoff, and Zhengyan D. Shi. “Holographic flows from CFT to the Kasner universe”. In: *JHEP* 08 (2020), p. 003. arXiv: 2004.01192 [hep-th].
- [15] Sean A. Hartnoll, Gary T. Horowitz, Jorrit Kruthoff, and Jorge E. Santos. “Gravitational duals to the grand canonical ensemble abhor Cauchy horizons”. In: *JHEP* 10 (2020), p. 102. arXiv: 2006.10056 [hep-th].
- [16] Sean A. Hartnoll, Gary T. Horowitz, Jorrit Kruthoff, and Jorge E. Santos. “Diving into a holographic superconductor”. In: *SciPost Phys.* 10.1 (2021), p. 009. arXiv: 2008.12786 [hep-th].
- [17] Charles W. Misner. “Mixmaster universe”. In: *Phys. Rev. Lett.* 22 (1969), pp. 1071–1074.
- [18] V. A. Belinsky, I. M. Khalatnikov, and E. M. Lifshitz. “Oscillatory approach to a singular point in the relativistic cosmology”. In: *Adv. Phys.* 19 (1970), pp. 525–573.
- [19] Lewis Sword and David Vegh. “Kasner geometries inside holographic superconductors”. In: *JHEP* 04 (2022), p. 135. arXiv: 2112.14177 [hep-th].
- [20] Seyed Ali Hosseini Mansoori, Li Li, Morteza Rafiee, and Matteo Baggioli. “What’s inside a hairy black hole in massive gravity?” In: *JHEP* 10 (2021), p. 098. arXiv: 2108.01471 [hep-th].
- [21] Mirmani Mirjalali, Seyed Ali Hosseini Mansoori, Leila Shahkarami, and Morteza Rafiee. “Probing inside a charged hairy black hole in massive gravity”. In: (June 2022). arXiv: 2206.02128 [hep-th].
- [22] Yan Liu, Hong-Da Lyu, and Avinash Raju. “Black hole singularities across phase transitions”. In: *JHEP* 10 (2021), p. 140. arXiv: 2108.04554 [hep-th].
- [23] Marc Henneaux. “The final Kasner regime inside black holes with scalar or vector hair”. In: *JHEP* 03 (2022), p. 062. arXiv: 2202.04155 [hep-th].
- [24] Oscar J. C. Dias, Gary T. Horowitz, and Jorge E. Santos. “Inside an Asymptotically Flat Hairy Black Hole”. In: (Oct. 2021). arXiv: 2110.06225 [hep-th].
- [25] Nicolás Grandi and Ignacio Salazar Landea. “Diving inside a hairy black hole”. In: *JHEP* 05 (2021), p. 152. arXiv: 2102.02707 [gr-qc].
- [26] Yan Liu and Hong-Da Lyu. “Interior of helical black holes”. In: *JHEP* 09 (2022), p. 071. arXiv: 2205.14803 [hep-th].
- [27] Elena Caceres, Arnab Kundu, Ayan K. Patra, and Sanjit Shashi. “Trans-IR flows to black hole singularities”. In: *Phys. Rev. D* 106.4 (2022), p. 046005. arXiv: 2201.06579 [hep-th].
- [28] Elena Caceres and Sanjit Shashi. “Anisotropic Flows into Black Holes”. In: (Sept. 2022). arXiv: 2209.06818 [hep-th].

- [29] Rong-Gen Cai, Li Li, and Run-Qiu Yang. “No Inner-Horizon Theorem for Black Holes with Charged Scalar Hairs”. In: *JHEP* 03 (2021), p. 263. arXiv: 2009.05520 [gr-qc].
- [30] Rong-Gen Cai, Chenghu Ge, Li Li, and Run-Qiu Yang. “Inside anisotropic black hole with vector hair”. In: *JHEP* 02 (2022), p. 139. arXiv: 2112.04206 [gr-qc].
- [31] Sean A. Hartnoll and Navonil Neogi. “AdS Black Holes with a Bouncing Interior”. In: (Sept. 2022). arXiv: 2209.12999 [hep-th].
- [32] Yu-Sen An, Li Li, Fu-Guo Yang, and Run-Qiu Yang. “Interior structure and complexity growth rate of holographic superconductor from M-theory”. In: *JHEP* 08 (2022), p. 133. arXiv: 2205.02442 [hep-th].
- [33] Wolfram Research Inc. *Mathematica, Version 12.3*. Champaign, IL, 2021.
- [34] Christopher P. Herzog and Silviu S. Pufu. “The Second Sound of SU(2)”. In: *JHEP* 04 (2009), p. 126. arXiv: 0902.0409 [hep-th].
- [35] Rong-Gen Cai, Li Li, and Li-Fang Li. “A Holographic P-wave Superconductor Model”. In: *JHEP* 01 (2014), p. 032. arXiv: 1309.4877 [hep-th].
- [36] Vijay Balasubramanian and Per Kraus. “A Stress tensor for Anti-de Sitter gravity”. In: *Commun. Math. Phys.* 208 (1999), pp. 413–428. arXiv: hep-th/9902121.
- [37] Sebastian de Haro, Sergey N. Solodukhin, and Kostas Skenderis. “Holographic reconstruction of space-time and renormalization in the AdS / CFT correspondence”. In: *Commun. Math. Phys.* 217 (2001), pp. 595–622. arXiv: hep-th/0002230.
- [38] E. E. Donets, D. V. Galtsov, and M. Yu. Zotov. “Internal structure of Einstein Yang-Mills black holes”. In: *Phys. Rev. D* 56 (1997), pp. 3459–3465. arXiv: gr-qc/9612067.
- [39] Peter Breitenlohner, George V. Lavrelashvili, and Dieter Maison. “Mass inflation and chaotic behavior inside hairy black holes”. In: *Nucl. Phys. B* 524 (1998), pp. 427–443. arXiv: gr-qc/9703047.